


ARTICLE

<https://doi.org/10.1038/s42004-019-0248-7>

OPEN

Facile and reversible digestion and regeneration of zirconium-based metal-organic frameworks

Jun Chu¹, Fu-Sheng Ke¹, Yunxiao Wang¹, Xiangming Feng², Weihua Chen², Xinping Ai¹, Hanxi Yang¹ & Yuliang Cao ^{1*}

The digestion/regeneration of metal-organic frameworks (MOFs) has important applications for catalysis, drug delivery, environmental decontamination, and energy storage, among other applications. However, research in this direction is limited and very challenging. Here, we develop a facile method to digest and regenerate a series of zirconium-based metal-organic frameworks (Zr-MOFs) by bicarbonate or carbonate salts. As an example, UiO-66 demonstrates well the mechanism of reversible digestion/regeneration processes. By analyzing the digested zirconium species via X-ray diffraction, Fourier transform infrared spectroscopy and Raman scattering spectroscopy, a digestion mechanism based on the formation of dissoluble complexes $[\text{Zr}_2(\text{OH})_2(\text{CO}_3)_4]^{2-}$ is proposed. Impressively, ultrafine Pd nanoparticles can be extracted from Pd@PCN-224 via this strategy. This work, thus, may provide new insight for the development of renewable MOFs and their practical applications.

¹College of Chemistry and Molecular Science, Hubei Key Laboratory of Electrochemical Power Sources and Savage Center for Molecular Sciences, Wuhan University, 430072 Wuhan, China. ²College of Chemistry and Molecular Engineering, Zhengzhou University, 450001 Zhengzhou, China.

*email: ylcao@whu.edu.cn

Metal-organic frameworks (MOFs) are emerging porous materials that have shown promise in cancer therapy^{1,2}, catalysis^{3–5}, chemical sensing^{6,7}, and energy-storage applications^{8–11}, including as electrodes,^{12–20} separators^{21,22}, and electrolytes²³, due to their high surface area²⁴, abundant ordered pores²⁵, and tailored pore environment²⁶. Zirconium-based MOFs (Zr-MOFs) are promising framework materials for practical applications because of their higher thermal and chemical stability compared with other MOFs^{27,28}. However, the durable skeletons hinder their future development as matrices for nanoparticles^{29,30} or quantum dots, reusable ligands, drug delivery systems³¹, and the component analysis of multivariate Zr-MOFs, where the framework should be completely removed. Although Zr-MOF digestion has been studied in aqueous solution with strong acids or corrosive or oxidizing reagents (i.e., HCl, HNO₃, HF, and CeF₃)^{32–35}, they are difficult to thoroughly dissolve even under such harsh conditions, which restricts their practical applications. Meanwhile, the regeneration of MOFs may offer access to cost-efficient and eco-friendly applications, but only few MOFs (such as MOF-5 and HKUST-1) have been investigated^{36–38}. Furthermore, the structures of these regenerated MOFs are unstable in moisture. Therefore, it is greatly needed to explore facile and efficient methods to digest and regenerate rigid MOFs, such as Zr-MOFs.

Here, we provide a facile, cost-efficient, and environmentally friendly approach for reversible digestion/regeneration of Zr-MOFs by use of bicarbonate or carbonate solutions. UiO-66, a classical Zr-MOF consisting of zirconium-oxo cluster and 1,4-benzenedicarboxylic acid (BDC), is selected to complete the digestion–regeneration circle. On the other hand, ligand recycling and Pd nanocatalyst synthesis can be achieved from Pd@PCN-224 (palladium nanoparticles are embedded in PCN-224, which is a Zr-MOF) based on this digestion approach. In addition, a digestion mechanism actuated by entropy change is discussed based on the formation of dissoluble complexes [Zr₂(OH)₂(CO₃)₄]^{2–} for Zr-MOF digestion process.

Results and discussion

Digestion and regeneration of UiO-66. A typical digestion–regeneration process of Zr-MOFs is illustrated in Fig. 1a. When the pristine UiO-66 (denoted as UiO-66-P in following paragraphs) particles are immersed in ammonium bicarbonate aqueous solution at room temperature, a colorless transparent solution is observed, suggesting a successful digestion process. To realize the regeneration of the dissolved UiO-66-P, the pellucid solution is treated with acetate acid and then evaporated. The residual white powders could transform into UiO-66 crystals with the help of *N,N*-dimethylformamide (DMF) and benzoic acid, which follows the same synthesis conditions as those of UiO-66-P (the detailed experiment processes are described in the “Methods” section and Supplementary Methods). The regenerated UiO-66 (denoted as UiO-66-R) shows powder X-ray diffraction (XRD) peaks of UiO-66-P, all of which can be indexed to UiO-66 diffraction pattern³⁹ in the Cambridge Crystallographic Data Center (CCDC) (Fig. 1b). Moreover, the isotherms of N₂ adsorption–desorption at 77 K for UiO-66-P and UiO-66-R were acquired (Fig. 1c). UiO-66-R shows specific surface area of 1247 m² g^{–1} and total pore volume of 0.59 cm³ g^{–1}, respectively, very close to those of UiO-66-P (1254 m² g^{–1} and 0.57 cm³ g^{–1}, respectively). Meanwhile, the pore size distribution reveals that the UiO-66-P and UiO-66-R samples have the same micropore size of ~1 nm (see Supplementary Figs. 1 and 2). They also have identical chemical bonds according to the Fourier transform-infrared spectroscopy (FTIR) spectra (see Supplementary Fig. 3). Thus, it is anticipated that the UiO-66-R has the same properties with UiO-66-P, implying that a complete digestion/regeneration process of Zr-MOF is successfully realized.

Besides, scanning electron microscopy (SEM) images in Fig. 1a show the agglomerated particle of UiO-66-R with the individual particle size of around 180 nm, which is smaller than UiO-66-P (around 300 nm). Moreover, it can be noted that the morphology of UiO-66-R is not perfect octahedral crystals as UiO-66-P, most likely due to the existence of water in reactant during regeneration reaction (see Supplementary Fig. 4)⁴⁰. In fact, regenerated Zr-MOF inherits the original surface area and structure, it may show comparable performance in practical application. Furthermore, PCN-224 with valuable porphyrin-based ligand has been digested and regenerated (the XRD and SEM images are shown in Supplementary Fig. 5), which indicates the feasibility of this digestion/regeneration method for general Zr-MOFs.

Factors influencing digestion. To understand the mechanism of Zr-MOF digestion, controlled experiments have been performed. First, the same mass of UiO-66-P was dispersed in HCl, CH₃COOH, NH₃·H₂O, and NaOH solutions with 1 M concentration (Fig. 2a), respectively. In consistent with previous reports^{31,41}, UiO-66-P can maintain its structure in neutral or acidic aqueous solution while being destroyed in alkaline solution (see Supplementary Fig. 6). But no matter what solution is tried, the degraded samples act as precipitates, illustrating that the pH value is not the reason for MOF digestion (further experiment is shown in Supplementary Fig. 8). Second, in order to reveal the effect of anions on the digestion of UiO-66-P, we replaced OH[–] by HCO₃[–], Cl[–], NO₃[–], and PO₄^{3–} of ammonium salts, as displayed in Fig. 2b. Amazingly, UiO-66-P can only be digested in NH₄HCO₃ solution, implying that the HCO₃[–] lays a critical role in UiO-66-P digestion. Furthermore, to verify the function of HCO₃[–], three more bicarbonate aqueous solutions, that is, LiHCO₃, NaHCO₃, and KHCO₃, were investigated (Fig. 2c). The results demonstrate that UiO-66-P can be completely dissolved in these bicarbonate aqueous solutions regardless of different cations. It further confirms that HCO₃[–] is the vital factor for the digestion process. In order to investigate the universality of the bicarbonate digestion method, Zr-MOFs with various organic ligands (their structures are shown in Supplementary Fig. 9), such as 1,2,4-benzenetricarboxylic acid (BDC-COOH), 1,4-naphthalene dicarboxylic acid (NDC), 2-bromobenzene-1,4-dicarboxylic acid (BDC-Br), and meso-*tetra*(4-carboxyphenyl)porphine (TCPP) (the corresponding MOFs are denoted by UiO-66-COOH, UiO-66-NDC, UiO-66-Br, and PCN-224) are employed to conduct the digestion experiment. All these Zr-MOFs can be degraded to form clear solution (Fig. 2d), which implies that this digestion process is determined by decomposition of zirconium-oxo clusters, but independent of the ligands. Thus, this digestion method is versatile for different Zr-MOFs, indicating a promising application of this digestion method in catalysis, drug delivery, and utilizing as matrices of nanoparticles.

Zirconium species in digested solution. In order to further understand the digestion mechanism of Zr-MOFs in bicarbonate aqueous solution, the digested zirconium species in the solution were systematically investigated. A digesting powder sample (denoted as FD sample) was gained by freeze drying (FD) the digested solution to prevent it from decomposing. Surprisingly, the dominated XRD peaks of FD sample in Fig. 3a are well matched with the reported diffraction pattern of ammonium zirconium carbonate (AZC) that is soluble in water, but unstable under high temperature⁴². This suggests that the carboxylic acid ligands and zirconium-oxo clusters transform into carboxylate ligands and AZC during the digestion process, respectively. Therefore, the AZC may be a possible digestion product of zirconium-oxo clusters. On the other hand, FTIR spectra were obtained to identify the chemical bond characteristics of the FD

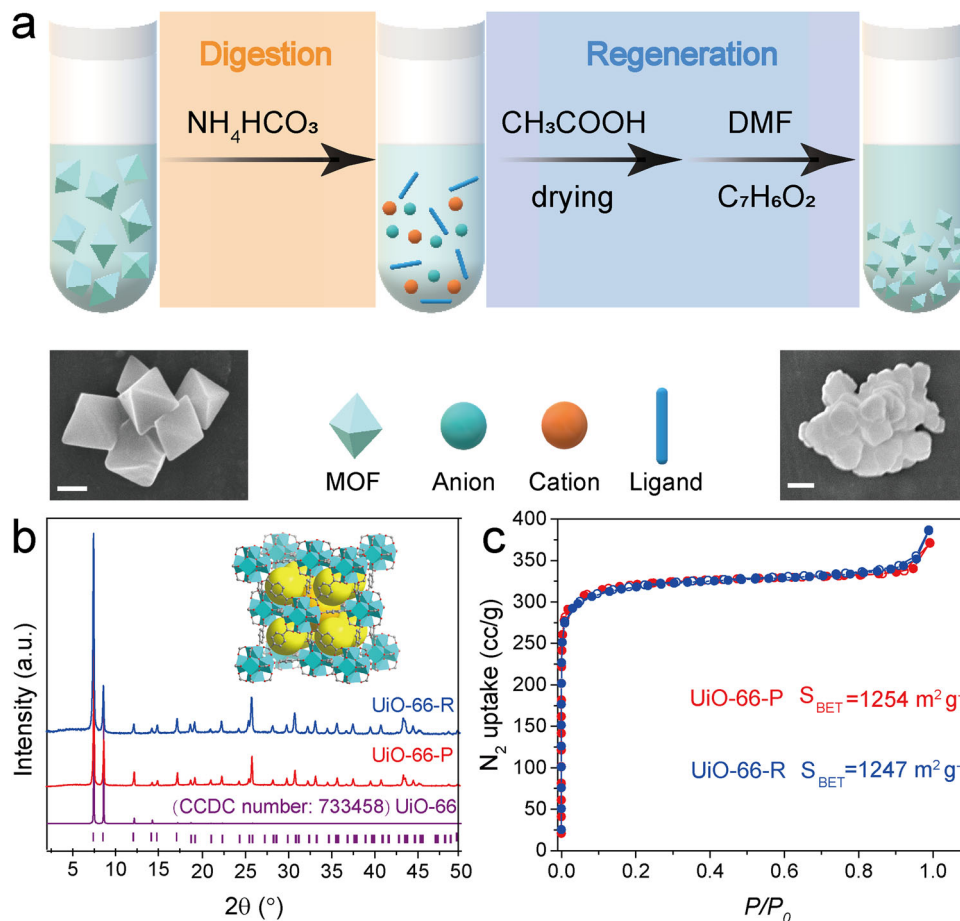


Fig. 1 Conceptual and experimental diagram of digestion and regeneration of UiO-66. **a** Schematic illustration for digestion/regeneration process of Zr-MOFs with SEM images of the UiO-66-P (left) and UiO-66-R (right) (scale bar: 200 nm). **b** XRD patterns of the reported UiO-66 (purple, CCDC number: 733458), UiO-66-P (red), and UiO-66-R (blue, inset: structure of UiO-66). **c** Isotherms of N₂ adsorption-desorption at 77 K (red: UiO-66-P; blue: UiO-66-R).

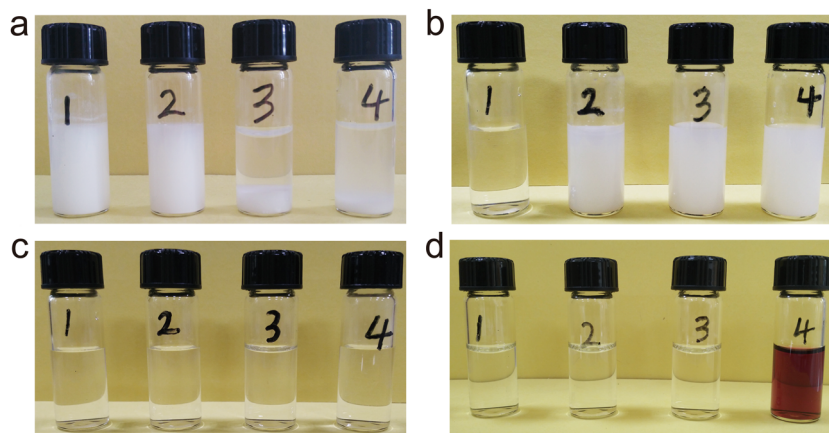


Fig. 2 Photographs of UiO-66-P digestion. **a** UiO-66-P immersed in HCl (1), CH₃COOH (2), NH₃•H₂O (3), and NaOH (4) aqueous solution. **b** UiO-66-P immersed in NH₄HCO₃ (1), NH₄Cl (2), NH₄NO₃ (3), and (NH₄)₃PO₄ (4) aqueous solution. **c** UiO-66-P immersed in NH₄HCO₃ (1), LiHCO₃ (2), NaHCO₃ (3), and KHCO₃ (4). **d** UiO-66-COOH (1), UiO-66-NDC (2), UiO-66-Br (3), and PCN-224 (4) immersed in NH₄HCO₃ aqueous solution.

sample and FD-AZC powder (denoted as FD-AZC) (Fig. 3b). It is obvious that the FTIR feature of the FD sample is in good agreement with that of the FD-AZC, supporting the results of XRD (Fig. 3a). In addition, the bands (highlighted area in Fig. 3b) centered at 1356 and 1046 cm⁻¹ reflect the symmetric stretch vibration of O–C–O and the stretch vibration of C–O of CO₃²⁻

in AZC according to previous reports⁴³. These FTIR evidences confirm the existence of AZC. Furthermore, the Raman spectra of FD sample and FD-AZC powders are shown in Supplementary Fig. 10. Obviously, the peak at 1052 cm⁻¹ is assigned to the anion of AZC contained in CO₃²⁻ and Zr species⁴⁴. In addition, the Raman scattering signals of FD-AZC can all be found in the

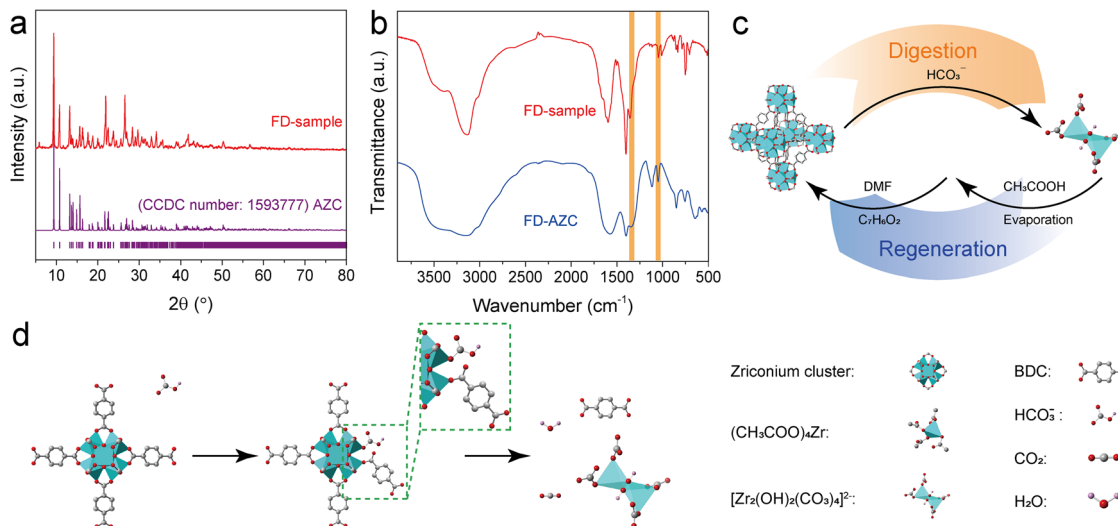
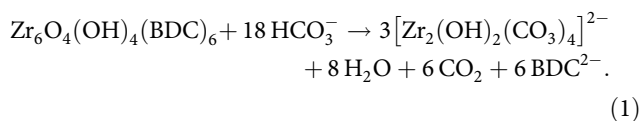


Fig. 3 Characterization of FD sample and diagram of Zr-MOF digestion. **a** XRD patterns of FD sample (red) and reported AZC (purple, CCDC number: 1593777). **b** FTIR spectra of FD sample (red) and FD-AZC (blue). **c** Schematic illustration for the digestion/regeneration process of Zr-MOFs. **d** Schematic illustration of a competition-digestion mechanism for UiO-66 via bicarbonate-mediated approach.

spectra of FD sample, which undoubtedly indicates the presence of AZC in solution.

Furthermore, proton nuclear magnetic resonance (¹H NMR) was utilized for the sake of clarifying the change in ligand (see Supplementary Fig. 11). The single peak located at around δ = 7.7 indicated the presence of terephthalate in D₂O. It revealed that BDC is released from UiO-66 with the existence of NH₄HCO₃, while it retained in the framework without the presence of bicarbonate. Therefore, UiO-66 is doubtlessly digested in NH₄HCO₃ aqueous solution.

Mechanism of Zr-MOF digestion. Based on the above discussion, a MOF digestion–regeneration cycle was promoted with a view to zirconium species evolution (Fig. 3c). First, zirconium-oxo clusters, [Zr₆O₄(OH)₄], exist in UiO-66 as metal sites. After adding NH₄HCO₃ aqueous solution, the soluble AZC is formed instead of zirconium-based clusters. Then, through the treatment of acetic acid and evaporation processes, UiO-66-R is emerged in DMF with the benzoic acid as a modulator via solvothermal method. Figure 3d shows a hypothetical competition–digestion mechanism of UiO-66. Like the deterioration mechanism of H₂O or OH⁻⁴¹, zirconium-oxo cluster is subject to the attack of HCO₃⁻, which takes place of the ligands coordinating with zirconium atoms. The ligands with carboxyl groups transfer into the corresponding salts; meanwhile, small molecules such as H₂O and CO₂ are generated. Because the structures of AZC are various and sensitive to the environment⁴⁴, we denoted herein the anions of AZC by [Zr₂(OH)₂(CO₃)₄]²⁻ based on the above results⁴². Thus, the chemical reaction for UiO-66 digestion could be written as



In addition, carbonate and citrate solutions can also digest UiO-66-P (see Supplementary Fig. 12a, the possible mechanism is shown in Supplementary Note 1), suggesting that forming a soluble complex with zirconium-oxo ions is a vital factor for the digestion of the UiO-66. Interestingly, we noted that the rate for digestion via carbonate and bicarbonate is much faster than that

of citrate (see Supplementary Fig. 12b, c). The time for UiO-66-P completely digested in NH₄HCO₃ solution to form the transparent solution is within 20 min (see Supplementary Fig. 12b), whereas in ammonium citrate solution it is up to 3 days (see Supplementary Fig. 12c). This phenomenon can be explained by Eyring equation

$$k = (k_B T/h) [\exp(-\Delta G^\ddagger/RT)] = (k_B T/h) [\exp(\Delta S^\ddagger/R) \exp(-\Delta H^\ddagger/RT)], \quad (2)$$

where k is the kinetic constant, k_B is the Boltzmann constant, R is the gas constant, T is the absolute temperature, h is the Planck constant, ΔG^\ddagger is the activation free energy, ΔH^\ddagger is the activation enthalpy, and ΔS^\ddagger the activation entropy. It indicates that the large kinetic constant (k) owes to the high activation entropy (ΔS^\ddagger). Thus, the digestion process performed in bicarbonate and carbonate aqueous solution produces much smaller molecules, especially the gas molecules (e.g., CO₂, Eq. 1, see Supplementary Eq. S1) than that in citrate aqueous solution (see Supplementary Eq. S4), resulting in a larger ΔS^\ddagger . Thus, the reaction rate in bicarbonate and carbonate solution is faster. Therefore, a competition–digestion mechanism actuated by entropy change could be suggested: Zr-MOF digestion occurred via the competing reactions between guest molecules and ligand molecules to form soluble species with metal-oxo clusters and low-molecular-weight products. For Zr-MOF digestion, three issues ought to be noticed: (1) the coordination ability of guest molecules should be stronger than ligands; (2) the digestion products are soluble in solvent; (3) generation of small-molecule products, particularly gases, can be beneficial to the digestion process due to larger entropy change.

Furthermore, for the regeneration process, a probable mechanism is proposed according to the formation of UiO-66^{45–47}. After acid treatment and removal of CH₃COONH₄, NH₄HCO₃, and H₂O by heat, the BDC and Zr(CH₃COO)₄ are left. Then, Zr-based compounds are formed by coordinating with CH₃COO⁻, benzoic acid, and H₂O in solvothermal procedure. Subsequently, UiO-66-R is generated via the ligand exchange between BDC and the ligands of Zr complex compound. The possible chemical

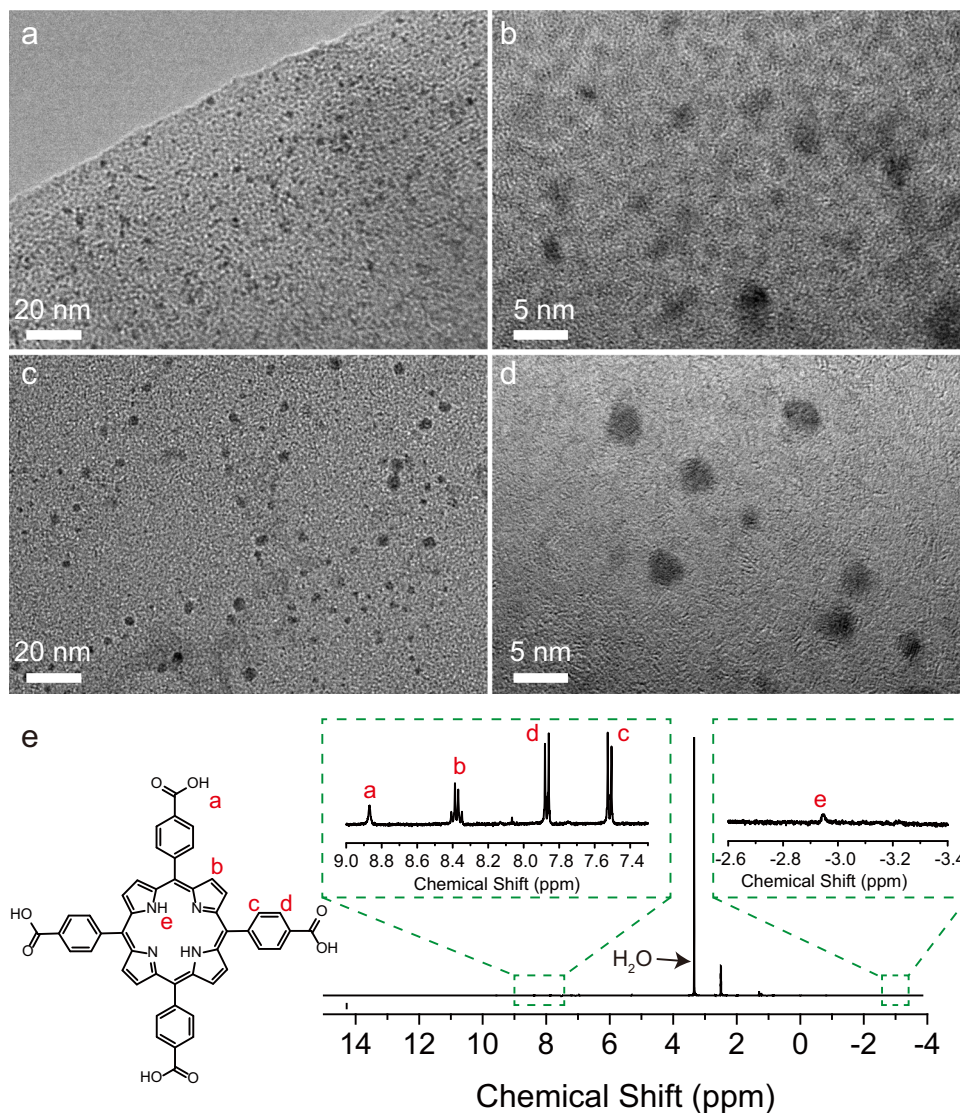


Fig. 4 Pd nanoparticles and ligand extraction from Pd@PCN-224. **a, b** TEM images of Pd@PCN-224. **c, d** TEM images of Pd nanoparticles extracted from the digested Pd@PCN-224 solution. **e** ^1H NMR spectra of recycled TCPP.

reactions during regeneration of UiO-66 are suggested in Supplementary Note 2.

Pd nanoparticles and ligand extraction. PCN-224, with Zr-based cluster and TCPP ligand, is a promising template and catalyst because of its applicable pore size and functional porphyrin-based ligand^{48–50}. Hence, to further verify the application feasibility of the digestion process, Pd@PCN-224 (see Supplementary Fig. 7) was utilized for metal nanoparticle retrieval and ligand recycle. Figure 4a, b shows clearly well-dispersed Pd nanoparticles (2–3 nm) in Pd@PCN-224. After treating with 0.1 M NH_4HCO_3 solution, Pd@PCN-224 is digested and the nanoparticles are successfully exposed from the dissolved frameworks (Fig. 4c, d). It can be obviously found that the Pd nanoparticles extracted from PCN-224 retain their pristine size and morphology, without any aggregation (Fig. 4c, d). In addition, the TCPP ligand recycle experiment was also performed on PCN-224. The TCPP ligand obtained by PCN-224 digestion and acid treatment was verified by ^1H NMR spectra (Fig. 4e). It indicates that this digestion method is feasible and has great

potential applications in the synthesis of single-dispersed metal catalysts, catalyst recycle, and regeneration of expensive MOFs.

In conclusion, a facile, cost-efficient, environmentally friendly method for Zr-MOF digestion/regeneration has been developed by utilizing bicarbonate/carbonate solution. As a result, the digested products are all soluble in water, and the regenerated MOF samples have the same structure, specific surface area, and pore structure with their parent MOFs. Well-dispersed Pd nanoparticles were obtained by the digestion process of Pd@PCN-224 to verify the feasibility of the method. To our knowledge, it is the first case of the complete digestion/regeneration of Zr-MOFs. Besides, by analyzing the dynamics of digestion process in bicarbonate and citrate solution, a competition–digestion mechanism actuated by entropy change has been promoted. This facile digestion procedure provides a novel insight for not only ligand recycle, component analysis, nanoparticle synthesis, and drug release but also chemical sensors, extraction–separation, and synthesis materials with unique nanostructure. Although the further optimization and exploration of regeneration process are needed, this novel digestion/regeneration method sheds light on a general MOF

digestion and regeneration process and provides access to future applications of MOFs.

Methods

Synthesis of UiO-66-X (X = P, COOH, Br, and NDC). The mixture of BDC (or BDC-COOH, BDC-Br, and NDC), $ZrOCl_2 \cdot 8H_2O$, benzoic acid, and DMF (mole ratio = 2:1:30:91) were sealed in an autoclave. After heating in an isothermal oven at 150 °C for 48 h, the white powder was collected via centrifugation. The product was washed with DMF and ethanol, and then dried at 60 °C under vacuum.

Synthesis of UiO-66-R. In all, 0.200 g of UiO-66-P was digested with 5 mL of 1 M NH_4HCO_3 aqueous solution. After that, 5 mL of 1 M CH_3COOH aqueous solution was added into the digestion solution, followed by an evaporation process. Then, the white powdery residue and 3.154 g of benzoic acid (25.82 mmol) were dissolved in 6 mL of DMF in a vial. Subsequently, the solution was transferred into an autoclave and heated in an isothermal oven at 150 °C for 48 h. Then, the synthesized UiO-66-R was washed with DMF and ethanol three times, respectively, and finally dried under vacuum at 60 °C.

Synthesis of PCN-224. In all, 0.06 g of $ZrCl_4$ (1.73 mmol), 0.02 g of TCPP (0.86 mmol), and 0.80 g of benzoic acid (25.88 mmol) were dissolved in 4 mL of DMF in a pyrex vial and stirred until the solid was dissolved. Then, the solution was heated in an isothermal oven at 120 °C for 36 h. After centrifugation, the product was washed with DMF and methanol three times, respectively, and finally dried under vacuum at 60 °C.

Synthesis of PCN-224-R. In all, 0.020 g of PCN-224 was digested with 2 mL of 1 M NH_4HCO_3 aqueous solution. After that, 2 mL of 1 M CH_3COOH aqueous solution was added into the digestion solution, followed by an evaporation process. Then, the dark-red powdery residue and 0.478 g of benzoic acid were dissolved in 2.5 mL of DMF in a vial. Subsequently, the solution was transferred into an autoclave and heated in an isothermal oven at 120 °C for 36 h. Then, the synthesized PCN-224-R was washed with DMF and ethanol three times, respectively, and finally dried under vacuum at 60 °C.

Synthesis of Pd@PCN-224. In all, 0.025 g of PCN-224 was ultrasonically dispersed in 1 mL of ethylene glycol and then preheated at 120 °C for 10 min. After that, 47 μ L of 0.6 M PVP and 23 μ L of 6 mM $PdCl_2$ aqueous solution was added to the ethylene glycol every 30 s with constant vigorous stirring (total volumes for PVP and $PdCl_2$ solutions are 1500 and 750 μ L, respectively). The resulting mixture was kept at 120 °C for an additional 10 min and then cooled down to room temperature. The obtained product was washed thoroughly several times with water and ethanol. The synthesized sample was further dried overnight under vacuum at 60 °C.

Digestion experiment. Zr-MOFs were immersed in 1 M salt aqueous solution, after which ultrasonic treatment was performed for 20 min.

TCPP recycle. Ten milligrams of PCN-224 was immersed in 3 mL of 1 M NH_4HCO_3 aqueous solution, followed by ultrasonic treatment. After complete digestion, 0.1 M HCl was added into the solution drop by drop until no more precipitation was generated. The products were collected by centrifugation and washed with water several times, and finally dried overnight at 80 °C.

XRD measurement. XRD data were recorded on a Rigaku Miniflex600 diffractometer operated at 40 kV, 15 mA for $Cu K\alpha$ ($\lambda = 1.5406 \text{ \AA}$) with a scan speed of 5°/min and a step size of 0.02° in 2θ at ambient temperature and pressure.

N_2 adsorption experiments. N_2 adsorption experiments were measured on a micromeritics ASAP 2020 HD88 physisorption instrument. A liquid nitrogen bath (77 K) was used for isotherm measurements. High-purity grade N_2 was used in the adsorption experiments. Before performing the analysis, the sample was outgassed at 150 °C under vacuum for 15 h. The multipoint BET analysis was performed by plotting $1/v(1 - P/P_0)$ versus P/P_0 ($P_0 = 1 \text{ bar}$) and v is the volume of nitrogen adsorbed per gram of MOF at STP. Pore size distributions for MOFs were analyzed by using DFT theory for N_2 adsorption based on a carbon model.

SEM imaging. SEM measurements were performed on a Zeiss Merlin Compact with an accelerating voltage of 5 kV. The samples were placed on clean aluminum foil and sputtered with platinum.

Fourier transform-infrared spectra. All FTIR spectra were recorded on a Nicolet micro FTIR Spectrometer iN10 and samples were tableted with KBr powder.

Raman spectra. A Renishaw-RM1000 spectrometer equipped with a CCD detector was used for the Raman studies. A laser with a wavelength of 532 nm was applied for excitation. Raman spectra were gathered by using two scans of 10-s exposure each time.

1H NMR test. All of the 1H NMR data were collected on Bruker Avance III HD 400 MHz nuclear magnetic resonance spectrometer. For digestion, UiO-66 was immersed in D_2O solution with 1 M NH_4HCO_3 . Moreover, UiO-66 and BDC were immersed in D_2O with $NH_3 \cdot H_2O$ because of the poor solubility of BDC in water. For ligand recycle of PCN-224, the recycled TCPP was immersed in deuterated dimethylsulfoxide.

Data availability

The data supporting the findings of this study are available within the article and its Supplementary Information files, or from the corresponding authors on reasonable request.

Received: 4 September 2019; Accepted: 4 December 2019;
Published online: 09 January 2020

References

- Jiang, K. et al. Thermal stimuli-triggered drug release from a biocompatible porous metal-organic framework. *Chem. Eur. J.* **23**, 10215–10221 (2017).
- Park, J., Jiang, Q., Feng, D. & Zhou, H. C. Controlled generation of singlet oxygen in living cells with tunable ratios of the photochromic switch in metal-organic frameworks. *Angew. Chem. Int. Ed.* **55**, 7188–7193 (2016).
- Zhang, T., Manna, K. & Lin, W. Metal-organic frameworks stabilize solution-inaccessible cobalt catalysts for highly efficient broad-scope organic transformations. *J. Am. Chem. Soc.* **138**, 3241–3249 (2016).
- Liang, J. et al. Postsynthetic ionization of an imidazole-containing metal-organic framework for the cycloaddition of carbon dioxide and epoxides. *Chem. Sci.* **8**, 1570–1575 (2017).
- Rimoldi, M. et al. Catalytic zirconium/hafnium-based metal-organic frameworks. *ACS Catal.* **7**, 997–1014 (2017).
- Wang, Y., Liu, Q., Zhang, Q., Peng, B. & Deng, H. Molecular wise approach to create metal-binding sites in MOFs and detection of biomarkers. *Angew. Chem. Int. Ed.* **57**, 7120–7125 (2018).
- Zhang, Y. et al. Luminescent sensors based on metal-organic frameworks. *Coord. Chem. Rev.* **354**, 28–45 (2018).
- Wu, H. B. & Lou, X. W. Metal-organic frameworks and their derived materials for electrochemical energy storage and conversion: Promises and challenges. *Sci. Adv.* **3**, eaap9252 (2017).
- Guan, B. Y., Yu, X. Y., Wu, H. B. & Lou, X. W. Complex nanostructures from materials based on metal-organic frameworks for electrochemical energy storage and conversion. *Adv. Mater.* **29**, 1703614 (2017).
- Xu, J., Lawson, T., Fan, H., Su, D. & Wang, G. Updated metal compounds (MOFs, -S, -OH, -N, -C) used as cathode materials for lithium-sulfur batteries. *Adv. Energy Mater.* **8**, 1702607 (2018).
- Zou, G. et al. Metal-organic framework-derived materials for sodium energy storage. *Small* **14**, 1702648 (2018).
- Zou, F. et al. MOF-derived porous $ZnO/ZnFe_2O_4/C$ octahedra with hollow interiors for high-rate lithium-ion batteries. *Adv. Mater.* **26**, 6622–6628 (2014).
- Yu, L., Yang, J. F. & Lou, X. W. Formation of CoS_2 nanobubble hollow prisms for highly reversible lithium storage. *Angew. Chem. Int. Ed.* **55**, 13422–13426 (2016).
- Hu, H., Zhang, J., Guan, B. & Lou, X. W. Unusual formation of $CoSe$ @carbon nanoboxes, which have an inhomogeneous shell, for efficient lithium storage. *Angew. Chem. Int. Ed.* **55**, 9514–9518 (2016).
- Liu, J. et al. MOF-derived hollow Co_9S_8 nanoparticles embedded in graphitic carbon nanocages with superior Li-ion storage. *Small* **12**, 2354–2364 (2016).
- Zheng, J. et al. Lewis acid-base interactions between polysulfides and metal organic framework in lithium sulfur batteries. *Nano Lett.* **14**, 2345–2352 (2014).
- Li, W. et al. Confined amorphous red phosphorus in MOF-derived N-doped microporous carbon as a superior anode for sodium-ion battery. *Adv. Mater.* **29**, 1605820 (2017).
- Zou, G. et al. 3D hollow porous carbon microspheres derived from Mn-MOFs and their electrochemical behavior for sodium storage. *J. Mater. Chem. A* **5**, 23550 (2017).
- Zou, G. et al. N-rich carbon coated $CoSnO_3$ derived from in situ construction of a Co-MOF with enhanced sodium storage performance. *J. Mater. Chem. A* **6**, 4839 (2018).
- Wu, Y. et al. Amorphous red phosphorus embedded in sandwiched porous carbon enabling superior sodium storage performances. *Small* **14**, 1703472 (2018).

21. Bai, S., Liu, X., Zhu, K., Wu, S. & Zhou, H. Metal-organic framework-based separator for lithium-sulfur batteries. *Nat. Energy* **1**, 16094 (2016).
22. He, Y. et al. Simultaneously inhibiting lithium dendrites growth and polysulfides shuttle by a flexible MOF-based membrane in Li-S. *batteries. Adv. Energy Mater.* **8**, 1802130 (2018).
23. Bai, S. et al. High-power Li-metal anode enabled by metal-organic framework modified electrolyte. *Joule* **2**, 2117–2132 (2018).
24. Farha, O. K. et al. De novo synthesis of a metal-organic framework material featuring ultrahigh surface area and gas storage capacities. *Nat. Chem.* **2**, 944–948 (2010).
25. Li, P. et al. Bottom-up construction of a superstructure in a porous uranium-organic crystal. *Science* **356**, 624–627 (2017).
26. Deng, H. et al. Multiple functional groups of varying ratios in metal-organic frameworks. *Science* **327**, 846–850 (2010).
27. Howarth, A. J. et al. Chemical, thermal and mechanical stabilities of metal-organic frameworks. *Nat. Rev. Mater.* **1**, 15018 (2016).
28. Kandiah, M. et al. Synthesis and stability of tagged UiO-66 Zr-MOFs. *Chem. Mater.* **22**, 6632–6640 (2010).
29. Lu, G. et al. Imparting functionality to a metal-organic framework material by controlled nanoparticle encapsulation. *Nat. Chem.* **4**, 310–316 (2012).
30. Gao, X. et al. Casting nanoporous platinum in metal-organic frameworks. *Adv. Mater.* **31**, 1807553 (2019).
31. Chen, Y., Li, P., Modica, J. A., Drout, R. J. & Farha, O. K. Acid-resistant mesoporous metal-organic framework toward oral insulin delivery: protein encapsulation, protection, and release. *J. Am. Chem. Soc.* **140**, 5678–5681 (2018).
32. Garibay, S. J. & Cohen, S. M. Isorecticular synthesis and modification of frameworks with the UiO-66 topology. *Chem. Commun.* **46**, 7700–7702 (2010).
33. Servalli, M., Ranocchiaro, M. & Van Bokhoven, J. A. Fast and high yield post-synthetic modification of metal-organic frameworks by vapor diffusion. *Chem. Commun.* **48**, 1904–1906 (2012).
34. Castellanos, S. et al. Structural effects in visible-light-responsive metal-organic frameworks incorporating ortho-fluoroazobenzenes. *Chem. Eur. J.* **22**, 746–752 (2016).
35. Hintz, H. & Wuttke, S. Solvent-free and time efficient postsynthetic modification of amino-tagged metal-organic frameworks with carboxylic acid derivatives. *Chem. Mater.* **26**, 6722–6728 (2014).
36. Majano, G. et al. Solvent-mediated reconstruction of the metal-organic framework HKUST-1 ($\text{Cu}_3(\text{BTC})_2$). *Adv. Funct. Mater.* **24**, 3855–3865 (2014).
37. Han, S. & Lah, M. S. Simple and efficient regeneration of MOF-5 and HKUST-1 via acid-base treatment. *Cryst. Growth Des.* **15**, 5568–5572 (2015).
38. Sun, X. et al. A novel mechanochemical method for reconstructing the moisture-degraded HKUST-1. *Chem. Commun.* **51**, 10835–10838 (2015).
39. Cavka, J. H. et al. A new zirconium inorganic building brick forming metal organic frameworks with exceptional stability. *J. Am. Chem. Soc.* **130**, 13850–13851 (2008).
40. Schaate, A. et al. Modulated synthesis of Zr-based metal-organic frameworks: from nano to single crystals. *Chem. Eur. J.* **17**, 6643–6651 (2011).
41. DeCoste, J. B. et al. Stability and degradation mechanisms of metal-organic frameworks containing the $\text{Zr}_6\text{O}_4(\text{OH})_4$ secondary building unit. *J. Mater. Chem. A* **1**, 5642–5650 (2013).
42. Clearfield, A. The crystal structure of ammonium di- μ -hydroxo-di [triscarbonato-zirconate (IV)] tetrahydrate. *Inorg. Chim. Acta* **4**, 166–170 (1970).
43. Sako, R. & Sakai, J. Effect of curing temperature on coating structure and corrosion resistance of ammonium zirconium carbonate on galvanized steel surface. *Surf. Coat. Technol.* **219**, 42–49 (2013).
44. Takasaki, F. et al. A monomeric $[\text{Zr}(\text{CO}_3)_4]^{4-}$ complex in an ammonium zirconium carbonate aqueous solution studied by extended X-ray absorption fine structure, Raman and nuclear magnetic resonance spectroscopy. *Dalton Trans.* **44**, 645–652 (2015).
45. Ragon, F. et al. In situ energy-dispersive X-ray diffraction for the synthesis optimization and scale-up of the porous zirconium terephthalate UiO-66. *Inorg. Chem.* **53**, 2491–2500 (2014).
46. Goesten, M. G. et al. Evidence for a chemical clock in oscillatory formation of UiO-66. *Nat. Commun.* **7**, 11832 (2016).
47. Sang, X. et al. Ionic liquid accelerates the crystallization of Zr-based metal-organic frameworks. *Nat. Commun.* **8**, 175 (2017).
48. Usov, P. M. et al. Cooperative electrochemical water oxidation by Zr nodes and Ni-porphyrin linkers of a PCN-224 MOF thin film. *J. Mater. Chem. A* **4**, 16818–16823 (2016).
49. Chen, Y.-Z. et al. Singlet oxygen-engaged selective photo-oxidation over Pt nanocrystals/porphyrinic MOF: the roles of photothermal effect and Pt electronic state. *J. Am. Chem. Soc.* **139**, 2035–2044 (2017).
50. Huang, N. et al. Systematic engineering of single substitution in zirconium metal-organic frameworks toward high-performance catalysis. *J. Am. Chem. Soc.* **139**, 18590–18597 (2017).

Acknowledgements

This work was generously supported by the National Key R&D Program of China (No. 2016YFB0100200), the National Natural Science Foundation of China (Nos. 21673165, 21333007 and 21773176), and the supercomputing system in the Supercomputing Center of Wuhan University.

Author contributions

Y.C. proposed the conception and supervised the project; J.C. conducted experiments reported in the paper; J.C. and F.-S.K. wrote the original draft; F.-S.K., Y.W., and Y.C. reviewed and edited the paper; X.F. and W.C. gave constructive advice for experiments and writing; X.A., H.Y., and Y.C. provided the funding and resource assistance.

Competing interests

The authors declare no competing interests.

Additional information

Supplementary information is available for this paper at <https://doi.org/10.1038/s42004-019-0248-7>.

Correspondence and requests for materials should be addressed to Y.C.

Reprints and permission information is available at <http://www.nature.com/reprints>

Publisher's note Springer Nature remains neutral with regard to jurisdictional claims in published maps and institutional affiliations.



Open Access This article is licensed under a Creative Commons Attribution 4.0 International License, which permits use, sharing, adaptation, distribution and reproduction in any medium or format, as long as you give appropriate credit to the original author(s) and the source, provide a link to the Creative Commons license, and indicate if changes were made. The images or other third party material in this article are included in the article's Creative Commons license, unless indicated otherwise in a credit line to the material. If material is not included in the article's Creative Commons license and your intended use is not permitted by statutory regulation or exceeds the permitted use, you will need to obtain permission directly from the copyright holder. To view a copy of this license, visit <http://creativecommons.org/licenses/by/4.0/>.

© The Author(s) 2020